Earth and Planetary Science Letters 499 (2018) 278–290

Contents lists available at ScienceDirect

Earth and Planetary Science Letters

www.elsevier.com/locate/epsl

High-temperature inter-mineral Cr isotope fractionation: A comparison of ionic model predictions and experimental investigations of mantle xenoliths from the North China Craton

Ji Shen [a,*], Liping Qin [a,*], Ziyao Fang [a], Yingnan Zhang [a], Jia Liu [a], Wei Liu [b], Fangyue Wang [c], Yan Xiao [d], Huimin Yu [a], Shiqiang Wei [b]

[a] CAS Key Laboratory of Crust–Mantle Materials and Environments, School of Earth and Space Sciences, University of Science and Technology of China, Hefei 230026, China
[b] National Synchrotron Radiation Laboratory, University of Science Technology of China, Hefei 230026, China
[c] Ore Deposit and Exploration Centre (ODEC), School of Resources and Environmental Engineering, Hefei University of Technology, Hefei 230009, China
[d] State Key Laboratory of Lithospheric Evolution, Institute of Geology and Geophysics, Chinese Academy of Sciences, PO Box 9825, Beijing 100029, China

ARTICLE INFO

Article history:
Received 22 December 2017
Received in revised form 23 July 2018
Accepted 26 July 2018
Available online 7 August 2018
Editor: F. Moynier

Keywords:
chromium isotope
inter-mineral fractionation
ionic model
mantle xenolith
XANES

ABSTRACT

Recent works have proposed that chromium (Cr) isotopes could be fractionated during peridotite partial melting and basaltic magma crystallization. However, until now, inter-mineral Cr isotope fractionation behavior for major mantle minerals has been poorly constrained. To investigate the mechanism and magnitude of equilibrium inter-mineral Cr isotope fractionation and to explore its implications for planetary mantle and crust lithology evolutions, we performed a systematic study of equilibrium Cr isotope fractionation between major mantle minerals by coupling theoretical ionic modeling with laboratory isotope analyses of natural samples and Cr valence determinations by X-ray absorption near edge spectroscopy (XANES). The ionic model considers both charges and coordination environments of Cr species in mantle minerals, which have proven to be critical factors affecting inter-mineral isotope fractionation. The ionic modeling results predict a general order of spinel (Spl) > pyroxene (Py) ≥ olivine (Ol) in $^{53}Cr/^{52}Cr$. Systematic Cr isotope analyses of coexisting mantle minerals of seventeen peridotite xenoliths from Beiyan in the North China craton were performed. Chromium isotope results for different mineral pairs of lherzolites (e.g., $\Delta^{53}Cr_{Spl-Ol}$ of 0.11‰ to 0.16‰, $\Delta^{53}Cr_{Spl-Py}$ of 0.04‰ to 0.11‰ and $\Delta^{53}Cr_{Py-Ol}$ of 0.05‰ to 0.10‰ at 870 °C to 970 °C), document measurable and systematic inter-mineral Cr isotope fractionation, in excellent agreement with the modeling results predicted with XANES-determined $Cr^{2+}/\Sigma Cr$ values of the mineral separates. This fractionation order could essentially account for Cr isotope behaviors during partial melting and magmatic crystallization observed in terrestrial peridotites and lunar basalts.

In contrast, we found that metasomatisms could influence Cr isotope compositions of minerals from Beiyan metasomatized clinopyroxene- (Cpx-) rich lherzolites and wehrlites by means of mineral–melt interaction and/or kinetic diffusion, leading to disequilibrium inter-mineral Cr isotope fractionation.

1. Introduction

Chromium (Cr), is an essential transition metal and a moderately compatible element that tends to be present in much greater concentrations in ultra-mafic and mafic rocks than in other terrestrial reservoirs. Chromium is a redox-active element and could aid in obtaining a better understanding of oxygen fugacity in rock, fluid, or melt systems during high-temperature geological processes. Recent advances in high-precision Cr isotope analyses using the double-spike method, as well as thermal ionization mass spectrometry (TIMS) and multicollector-inductively coupled plasma mass spectrometry (MC–ICP–MS) instruments have generated some contradictory observations on Cr isotope fractionation during high-temperature geological processes, e.g., partial melting of mantle peridotites and fractional crystallization of basaltic magmas (Schoenberg et al., 2008; Bonnand et al., 2016; Xia et al., 2017). Schoenberg et al. (2008) first observed that mantle xenoliths, ultramafic cumulates, basaltic, and granitic rocks, have indistinguishable Cr isotope compositions [δ^{53}Cr values rang-

* Corresponding authors.
E-mail addresses: sjlcwqqq@ustc.edu.cn (J. Shen), lpqin@ustc.edu.cn (L. Qin).

https://doi.org/10.1016/j.epsl.2018.07.041
0012-821X/

ing from −0.21‰ to −0.02‰ relative to the National Institute of Standards and Technology (NIST) Standard Reference Material 979 (SRM979) Cr isotope standard], which may be taken as evidence of limited mineral–melt isotope fractionation. However, Farkaš et al. (2013) and Shen et al. (2015) observed that the mantle-derived chromites were isotopically heavier than the average Bulk Silicate Earth (BSE) and ultramafic rocks, suggesting potential fractionation during chromite crystallization. Recently, Xia et al. (2017) found distinguishable Cr isotope variations among worldwide mantle peridotite xenoliths, in which the more refractory ones tended to have heavier Cr isotopes. Furthermore, Bonnand et al. (2016) observed considerable Cr isotope fractionation during spinel (Spl) crystallization from lunar basaltic magma, which might be attributed to only Cr^{3+} incorporated into spinel and predominantly Cr^{2+} in lunar magmatic liquids. Overall, Cr isotope fractionation during high-temperature processes is not negligible, as originally thought (Schoenberg et al., 2008), and further studies are needed to elucidate high-temperature Cr isotope behaviors. To this end, determinations of equilibrium Cr isotope fractionation factors between major rock-forming minerals are necessary. Using theoretical and empirical predictions, Moynier et al. (2011) found that Cr^{3+}-bearing magnesiochromite was Cr isotopically heavier than Cr^{2+}-bearing olivine (~0.2‰ in $^{53}Cr/^{52}Cr$), at temperatures even greater than 800 °C. In our recent work (Shen et al., 2015), the coexisting clinopyroxenes (Cpx) and garnets (Gt) in two garnet clinopyroxenites displayed $\Delta^{53}Cr_{Cpx\text{-}Gt}$ ($\Delta^{53}Cr_{X\text{-}Y} = \delta^{53}Cr_X - \delta^{53}Cr_Y$) of 0.06‰ and 0.34‰, suggesting potential high-temperature inter-mineral Cr isotope fractionation. However, to date, there have been no systematic investigations of inter-mineral Cr isotope fractionation in mantle rocks, which hamper interpretation of the Cr isotope data for mantle-derived and lunar rocks, hindering further implications of the Cr isotope system in high-temperature processes.

Macris et al. (2015) and Young et al. (2015) proposed a revised ion model to interpret inter-mineral iron (Fe) isotope fractionation such that the reported data almost fall within the range defined by the model. According to the model, inter-mineral Fe isotope fractionation essentially depends on the different valence states and coordination numbers that affect Fe–O bond length and stiffness. A similar approach for inter-mineral Fe isotope fractionations was used by Sossi and O'Neill (2017), which quantified the degree to which the effects of coordination and oxidation state were independently of one another. Because Cr^{2+} and Fe^{2+}, Cr^{3+} and Fe^{3+} have identical charges and similar ionic radii (Shannon, 1976), they might behave similarly in mineral lattices, allowing the similar speculation for inter-mineral Cr isotope fractionation by model calculations. This method potentially provides a complementary approach to laboratory determination of equilibrium inter-mineral isotope fractionation factors. However, because Cr is often a trace element, whereas Fe is often a major element, it is necessary to test whether this model is also applicable to Cr isotopes.

Here, we present the first systematic determination of Cr isotope fractionation among major mantle minerals from the Beiyan peridotite xenoliths from the North China Craton. To further compare our data with theoretical predictions, we developed an ionic model for Cr following similar models for Fe proposed by Macris et al. (2015) and Young et al. (2015). Moreover, to explore the potential effect of Cr valence states on isotope fractionation, we performed quantitative analyses of $Cr^{2+}/\Sigma Cr$ values by X-ray absorption near edge spectroscopy (XANES) on thirteen mineral separates from these xenoliths.

2. Samples

Mineral separates studied here include olivine (Ol), orthopyroxene (Opx), clinopyroxene (Cpx), and spinel (Spl) from seventeen mantle xenoliths (including five lherzolites, seven Cpx-rich lherzolites, and five wehrlites from Xiao et al., 2010, 2013) hosted by Beiyan Cenozoic alkaline basalts (~19 Ma, Xu et al., 2012) in the North China Craton. The lherzolites have limited forsterite content variations of Ol (Fo ≈ 89.1–90.2) and show spoon-shaped to slightly light rare earth element (LREE) enrichment relative to heavy rare earth elements (HREEs), suggesting a low degree of melt extraction and weak metasomatisms (Xiao et al., 2010). The Cpx-rich lherzolites and wehrlites have low Fo contents of Ol (<88) and enriched LREE patterns, reflecting interaction of the lherzolites with enriched silicate melts (Xiao et al., 2010). The carbonate mineral inclusions, positive Ba and Sr anomalies and light Mg isotope compositions in the wehrlites imply the additional incorporation of recycling carbonatitic melt (Xiao et al., 2010, 2013).

All peridotite xenoliths were fresh and free of secondary alteration and basaltic veins inside. All samples were spinel facies with 1% to 2% spinel minerals, varying in modal compositions for lherzolites (68–73% Ol, 17–22% Opx, 8–10% Cpx, $n = 5$), Cpx-rich lherzolites (67–72% Ol, 8–18% Opx, 14–21% Cpx, $n = 7$), and wehrlites (62–68% Ol, 0–3% Opx, 29–34% Cpx, $n = 5$) (Xiao et al., 2013). Detailed major and trace element abundances of the investigated whole-rock peridotites and minerals have been published by Xiao et al. (2010, 2013). Briefly, Cr concentrations of Cpx in these peridotite xenoliths were higher than those of co-existing Opx, but lower than those in co-existing Spl [Cr_2O_3 of 0.28–1.24 wt.% for Cpx, 0.25–0.44 wt.% for Opx and 5.1–15.3 wt.% for Spl determined by electron probe from Xiao et al., 2013].

3. Analytical methods

3.1. Column chemistry and mass spectrometry

Fresh mineral grains were handpicked under a binocular microscope before dissolution. Dissolution of silicate minerals and column chemistry were performed following procedures described in previous studies (Qin et al., 2010; Trinquier et al., 2008). Here, we present a brief description: silicate mineral grains were dissolved in Savillex beakers in a combination of HF–HCl–HNO_3; Spl grains were ground to fine powders and dissolved in microwave oven in concentrated HCl–HNO_3 (3:1 in volume) following the same procedure by Xia et al. (2017). After complete sample digestion, Cr concentrations of the solutions were analyzed using ICP-MS to ensure that aliquots to be taken out and mixed with 1 ml ^{50}Cr–^{54}Cr double spike (concentrations of ^{50}Cr and ^{54}Cr are 2.716 nm/g and 1.742 nm/g, respectively) contained 1 μg Cr. Separation of Cr was achieved by performing the two-step cation exchange chromatography procedure (Qin et al., 2010; Trinquier et al., 2008), which involved isolating Cr from matrix elements with 1 M HCl in the primary column filled with 1 ml Bio-Rad 200–400 mesh AG50-X8 resin and with 2 M HCl in the clean-up column filled with 0.33 ml of the same resin. The procedure blanks were typically <3 ng, which was negligible.

Chromium isotope analyses of all minerals were performed using a Neptune Plus MC–ICP–MS instrument at the CAS Key Laboratory of Crust-Mantle Materials and Environments at the University of Science and Technology of China, Hefei. The sample solution was introduced with a PFA Aridus II^{TM} desolvating nebulizer system (CETAC Technologies). To minimize potential polyatomic interferences from $^{40}Ar^{14}N^+$ on ^{54}Cr, the desolvator was operated with only Ar gas without the addition of N_2. The uptake rate of the sample solution was 50 μL/min by Ar carrier gas with a flow rate of ~2.0 L/min. Both samples and standards were dissolved in 2% HNO_3 and diluted to 200 ppb to avoid instrumental "on-mass" background. Chromium isotope analyses were performed in medium to high resolution modes ($5500 < \Delta M/M < 11000$, Bonnand et al., 2016), which could effectively resolve

polyatomic interferences. Typical intensities of ^{52}Cr were 5–6 V in high resolution mode. In medium resolution mode, similar analytical set-up not only allows higher intensity of 12–15 V for ^{52}Cr, but also leads to significantly enhanced $^{40}Ar^{14}N^+$ and $^{40}Ar^{16}O^+$ signals. Thus, in order to minimize these interferences, intensities of ^{52}Cr for 200 ppb Cr solutions were generally adjusted to 6–7 V, achieving $^{52}Cr/^{40}Ar^{14}N^+ \geq 25$ and $^{52}Cr/^{40}Ar^{16}O^+ \geq 50$. During each analytical session, the spiked internal standard (SCP) was analyzed at intervals of 4–5 samples, and the spiked NIST SRM 3112a was analyzed at the beginning of each session. Each analysis consisted of a total of 4 blocks with 30 cycles per block. The long-term instrumental reproducibility was determined by measuring SCP relative to the NIST standard 979 over a long period between December 2014 and December 2017, giving a mean value of −0.02 ± 0.04‰ ($N = 655$, 2SD, Supplementary Table S1). The long-term reproducibility for rock samples was determined by monitoring the peridotite standard JP-1 (averaging at -0.10 ± 0.06‰) ($N = 26$, 2SD, Supplementary Table S1). Most samples were analyzed twice or more times during a single analytical session. The uncertainties quoted for individual sample analyses were conservatively defined as the largest of, the 2SD of the replicated sample measurements (or the 2SE of the internal uncertainty of single sample measurement when the sample was only analyzed once), the 2SD of the replicated standard measurements in the same session, and the long-term reproducibility of the peridotite standard JP-1. All Cr isotope results were reported relative to the NIST SRM979. Chromium isotope compositions of the NIST SRM 3112a and the reference rocks (e.g., BHVO-2, BIR, PCC-1) analyzed during the course of this study (Supplementary Table S1) were in good accord with those performed using TIMS (Shen et al., 2015; Xia et al., 2017) and with those from previous works (Schoenberg et al., 2008). Average Cr isotope composition of JP-1 (-0.10 ± 0.06‰, $n = 26$) was also in agreement with published values of repeated analyses of JP-1 (-0.13 ± 0.02‰, $n = 14$, Bonnand et al., 2016).

For comparison, mineral separates from three lherzolite samples (Cl09-62 and Cl09-74, Cl09-65), and one Cpx-rich lherzolite (Cl09-81) were analyzed using a Thermo Finnigan Triton multicollector TIMS at the Isotope Geochemistry Laboratory, China University of Geosciences, Beijing. The instrumental analytical protocol was described in our previous works (Qin et al., 2010; Xia et al., 2017). Repeated analyses of NIST SRM979 yielded $\delta^{53}Cr$ values of 0.00 ± 0.02‰ (2SD, $n = 3$). Samples were generally analyzed once (420 cycles) with a typical 2SE better than ±0.01‰. Low Cr concentrations or interferences from organic matters resulted in low signal intensities for some samples, thus larger 2SE values, e.g., ±0.03‰ for Cl09-74 Ol and ±0.09‰ for Cl09-81 Ol. The error assigned to the analyses by TIMS was the larger value of the 2SE of the individual sample analyses and the 2SD of the repeated standard analyses (0.02‰) in the same analytical session.

3.2. Method for X-ray absorption near edge spectroscopy (XANES) analysis

3.2.1. Sample preparation and instrument measurement

X-ray absorption near edge spectroscopy (XANES) at the Cr *K*-edge of the mineral samples and reference compounds were conducted at room temperature (~25 °C) at the Beijing Synchrotron Radiation Facility (BSRF) in China on the beamline 1W1B using a Si(111) double crystal monochromator. The synchrotron was operated at 2.5 GeV and 150 to 250 mA. The beam size of ~0.5 mm (horizontal) × ~0.5 mm (vertical) was controlled by using a slit in front of the source. Data for Cr metal foil as a non-valent Cr standard for energy calibration was obtained in transmission mode with a gas-filled ionization chamber. Trivalent Cr reference material $Cr(OH)_3$ was diluted to 1 wt.% Cr with graphite powder by grounding the mixture in an agate mortar for 30–60 min, and was then compressed to a tablet using a steel tablet press. All minerals for XANES analyses were hand-picked carefully under a binocular microscope to avoid inclusions. Cpx, Opx and Spl separates were diluted to ~1000 ppm Cr with graphite powder and compressed to individual tablets in the same fashion. To avoid cross contamination, the interfaces between the sample powder and the steel sheet were segregated by several dust-free wipes. Due to low Cr concentrations in Ol, approximately 0.5–1 g Ol separates from each sample were ground to powder without graphite and were pasted on a plastic tape. The X-ray absorption spectra of the standard and the minerals (including Ol), which were assembled at 45° angle to the X-ray beam, were acquired in fluorescence mode with a Lytle detector positioned orthogonally to the beam. The consistently low signal intensities of Ol, which were positively correlated with Cr concentrations, documented the absence of Spl or Py inclusions during analyses. Additionally, because low Cr contents in Ol lead to poor signals while using the Lytle detector, the Ol powders were measured using a 19-element Ge solid-state detector for fluorescence signals to lower the detection limit. All spectra were collected for the energy range of 5780–6340 eV. The energy step width was set to different values for individual energy regions, e.g., 30 eV in the far pre-edge region (5780–5910 eV), 5 eV in the near pre-edge region (5910–5940 eV), 0.5 eV in the near edge region (5940–6010 eV), 1 eV in the near post-edge region (6010–6090 eV) and 50 eV in the far post-edge region (6090–6340 eV). The energy was calibrated by defining the first derivative peak of Cr in the metal foil to be 5989 eV.

3.2.2. Data reduction

XANES spectra data were analyzed using Athena software. The spectra were normalized after energy calibration (Fig. 1a, c and e). Before derivation, the spectra of mineral separates were first smoothed with a three-iteration moving average because of poor signal-to-noise ratio (Bell et al., 2014). Based on the intensity differences of pre-edge peaks (1s–4s), and energy differences of main edges (derivative highest peaks) and edge crests (zero derivative points), among Cr^0, Cr^{2+}, Cr^{3+} and Cr^{6+}, individual Cr species in minerals could be preliminarily estimated (Sutton et al., 1993; Berry and O'Neill, 2004; Eeckhout et al., 2007). The key to quantitatively determine Cr^{2+} and Cr^{3+} proportions was the shoulder on the main Cr–*K* absorption edge. The intensities of this spectral feature were attributed to different capacities of 1s–4s electron transition for Cr^{2+} and Cr^{3+}. High-symmetry octahedral coordination of Cr^{3+} make the 1s–4s electron transition forbidden, while, Cr^{2+} occurring in a Jahn–Teller distorted environment allows such electron transition (Sutton et al., 1993). In the normalized program, the intensity of this shoulder at ~5994 eV on the *K* absorption edge of Cr was proposed to be directly correlated with Cr^{2+}/Cr^{3+} (or $Cr^{2+}/\Sigma Cr$) in minerals and silicate glasses (Berry and O'Neill, 2004). Thus, we used intensities of the spectral feature to determine the $Cr^{2+}/\Sigma Cr$ ratios in the mineral samples, which could be easily quantified from the derivative spectrum using either the area or the height of 1s–4s peak (Bell et al., 2014; Berry and O'Neill, 2004; Berry et al., 2006; Eeckhout et al., 2007; Goodrich et al., 2013; McKeown et al., 2014; Sutton et al., 1993). Replicate measurements of CLB05-15 Ol, for which the calculated $Cr^{2+}/\Sigma Cr$ ratios are 0.14 and 0.16, give an uncertainty of ~ ±0.014 (1σ). Bell et al. (2014) estimated the inherent uncertainty for calculated $Cr^{2+}/\Sigma Cr$ ratios using either the 1s–4s peak height or the area of XANES spectra to be approximately ±0.05 (1σ). Considering that the reference standards for $Cr^{2+}/\Sigma Cr$ calculations were from Bell et al. (2014), a potential uncertainty associated with the subjectivity of spectral normalization procedures was added, which

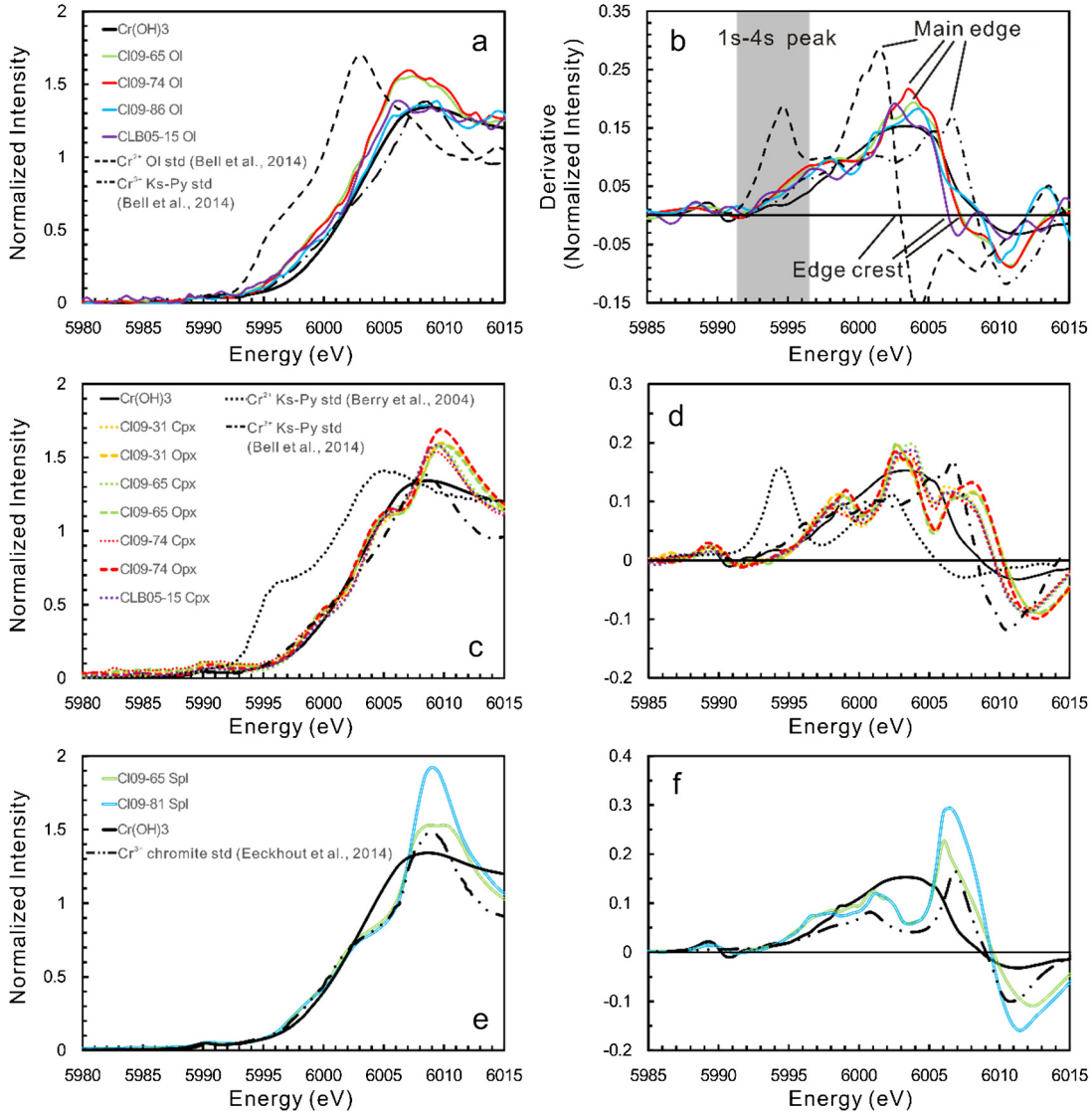

Fig. 1. Plot (a) presents the normalized Cr *K*-edge XANES spectra for Ol separates from two lherzlites Cl09-65, Cl09-74, one Cpx-rich lherzolite CLB05-15 and one wehrlite Cl09-86, as well as the spectra for the Cr metal (zero-valent Cr) and $Cr(OH)_3$ (trivalent Cr) standards. Plot (b) presents the corresponding derivative spectra. Plots (c) and (e) present the normalized Cr *K*-edge XANES spectra for Cpx and Opx, as well as Spl from the lherzolites and Cpx-rich lherzolites, respectively, while plots (d) and (f) present the corresponding derivative spectra. The integral range used to determine the area of the 1s→4s peaks in the derivative spectra is also shown by the gray area. The reference standards in (a) and (b) for Ol minerals are the Cr^{2+}-bearing ureilite Ol ($Cr^{2+}/\Sigma Cr = 0.95$) and the Cr^{3+} feldspar–pyroxene (Fs–Pl) silicate glass ($Cr^{2+}/\Sigma Cr = 0$) from Bell et al. (2014), while the standards in (c) and (d) for Py minerals are two feldspar–pyroxene (Fs–Py) silicate glass with $Cr^{2+}/\Sigma Cr$ values of 0 and 1 from Berry and O'Neill (2004) and Bell et al. (2014). The Spl standard is derived from the chromite ($Cr^{2+}/\Sigma C = 0$) from Eeckhout et al. (2007) in (e) and (f).

was estimated to be $\sim \pm 0.05$ (1σ) in valences (Goodrich et al., 2013). Taken together, the error for the calculated $Cr^{2+}/\Sigma Cr$ values in this work is conservatively assigned to be ± 0.10 (1σ).

The analytical methods for mineral major and trace elements are presented in Appendix A in detailed.

4. Results

4.1. Chromium isotope compositions of minerals

Chromium isotope compositions for the standards and the mineral separates (Ol, Opx, Cpx and Spl), along with the mineral modes, the Fe/Mg ratios of these minerals, the Ca/Al ratios of Cpx, the equilibrium temperatures, and the calculated oxygen fugacities for these peridotites are present in Supplementary Table S1. The chemical compositions of the minerals and the equilibrium temperature calculations are from Xiao et al. (2013). The equilibrium temperatures of two unreported samples (Cl09-65 and Cl09-81) are estimated by two-pyroxene Fe–Mg thermometry (Wells, 1977). The oxygen fugacities for the lherzolites and Cpx-rich lherzolites were calculated according to the modified Ol–Opx–Spl oxygen geobarometer by Ionov and Wood (1992).

The mineral separates display large Cr isotope variations within each type of minerals, with $\delta^{53}Cr$ ranging from −0.43‰ to 0.09‰ in Ol, −0.32‰ to 0.14‰ in Cpx, −0.32‰ to 0.19‰ in Opx, and −0.33‰ to 0.23‰ in Spl (Supplementary Table S1); Ol tends to be the lightest in $\delta^{53}Cr$. The $\Delta^{53}Cr_{Cpx-Ol}$, $\Delta^{53}Cr_{Opx-Ol}$ and $\Delta^{53}Cr_{Spl-Ol}$ values range from $-0.06‰ \pm 0.08‰$ to $0.36‰ \pm 0.08‰$, $-0.07‰ \pm 0.13‰$ to $0.20‰ \pm 0.08‰$, and $-0.14‰ \pm 0.08‰$ to $0.39‰ \pm 0.08‰$, respectively (Table 1). The Cr isotope results of repeated minerals from lherzolites Cl09-74 and Cl09-62 by TIMS were in good agreement with those by MC–ICP–MS within errors (Supplementary Table S1). The consistent results further confirm that our analyses were precise and accurate.

Table 1
Inter-mineral Cr isotope fractionations (‰) in Beiyan peridotites.

Sample	Rock	$\Delta^{53}Cr_{Spl-Ol}$	$\Delta^{53}Cr_{Opx-Ol}$	$\Delta^{53}Cr_{Cpx-Ol}$	$\Delta^{53}Cr_{Opx-Cpx}$
Cl09-31	Lherzolite	0.14	0.08	0.07	0.01
Cl09-62	Lherzolite	−0.04	0.19	−0.02	0.21
			0.16[a]	−0.03[a]	0.19[a]
Cl09-65	Lherzolite	0.14[a]	0.10[a]	0.05[a]	0.05[a]
Cl09-73	Lherzolite	0.16	0.05	0.08	−0.03
Cl09-74	Lherzolite	0.11	0.03	0.06	−0.03
		0.09[a]	0.05[a]	0.07[a]	0.01[a]
Cl09-06	Cpx-rich lherzolite	−0.14	0.10	0.06	0.04
Cl09-33	Cpx-rich lherzolite			0.23	
Cl09-35	Cpx-rich lherzolite		0.20	0.36	−0.16
Cl09-47	Cpx-rich lherzolite	0.26	0.06	0.20	−0.14
Cl09-75	Cpx-rich lherzolite	0.24	0.13	0.16	−0.03
Cl09-81	Cpx-rich lherzolite	0.31[a]	−0.05[a]	0.04[a]	−0.11[a]
CLB05-15	Cpx-rich lherzolite	0.23	0.05	0.12	−0.07
Cl09-78	Wehrlite	0.39		0.01	
Cl09-82	Wehrlite			−0.06	
Cl09-84	Wehrlite	0.25		0.16	
Cl09-86	Wehrlite	0.15		0.07	
Cl09-87	Wehrlite			0.25	

[a] The value represents Cr isotope data performed by TIMS.

4.2. Chromium valence states in mantle minerals

Fig. 1a presents the normalized Cr *K*-edge spectra for the standards [Cr metal, $Cr(OH)_3$] and four Ol separates from two lherzolites Cl09-65 and Cl09-74, one Cpx-rich lherzolite CLB05-15 and one wehrlite Cl09-86. The spectra of two synthetic standards with $Cr^{2+}/\Sigma Cr = 0$ (a silicate glass) and 0.95 (an ureilite Ol) from Bell et al. (2014) are also plotted for comparison purposes. Sutton et al. (1993) has pointed that the Cr^{2+} spectra for both the synthetic Cr^{2+}-doped forsterite and the silicate glass show leftward energy shifts in the main peak and the crest edge by 3 to 5 eV relative to spectra for two Cr^{3+} standards in the derivative spectrum (e.g., Fig. 1b). Additionally, energies of the main peak and the crest edge for Ol with higher $Cr^{2+}/\Sigma Cr$ ratios were more close to those for Cr^{2+} standards (Bell et al., 2014; Berry and O'Neill, 2004; Berry et al., 2006; Sutton et al., 1993). In the derivative spectrum (Fig. 1b), significantly rightward shifts of edge crest and main edge energies of Cl09-86 Ol, which overlap those of the $Cr(OH)_3$ standard and referenced Cr^{3+} silicate standard from Bell et al. (2014), imply absence of Cr^{2+}. By contrast, the Ol spectra from Cl09-65, Cl09-74 and CLB05-15 show higher 1s–4s peaks at ~5994 eV, and medium energies of edge crest and main edge between Cr^{2+} and Cr^{3+} standards, indicating the presences of Cr^{2+} in these Ol separates. According to simple linear mixing of the heights of the 1s–4s peaks for Cr^{2+} and Cr^{3+} in the derivative spectra (Bell et al., 2014; Berry and O'Neill, 2004; Berry et al., 2006), the calculated $Cr^{2+}/\Sigma Cr$ ratios of Ol separates from Cl09-65, Cl09-74 and CLB05-15 are 0.18, 0.20 and 0.16, respectively (Table 2). For comparison, the $Cr^{2+}/\Sigma Cr$ ratios are re-calculated by using the area of the 1s–4s peaks, by integrating the peak intensity for energy interval from 5991.3 eV to 5996.3 eV (Bell et al., 2014; Berry and O'Neill, 2004). The calculated results of $Cr^{2+}/\Sigma Cr$ ratios are nearly identical to those calculated using the peak height method (Table 2). With respect to all Py and Spl separates (including four Cpx, three Opx and two Spl), no Cr^{2+} is detected, as evidenced by their low 1s–4s peaks and right shifts of edge crests similar to Cr^{3+} standards (Fig. 1c–f).

4.3. Major and trace element data of minerals

The major elements of individual minerals from unreported Cl09-65 and Cl09-81 in Xiao et al. (2013) are presented in Supplementary Table S2 (Appendix A). Elemental profiles (major and trace elements) for individual Opx minerals from two lherzolites Cl09-62 and Cl09-73 are presented in Supplementary Table S3.

Table 2
The height ($H_{1s/4s}$) and area (A_{1s-4s}) of 1s–4s derivative peak and calculated $Cr^{2+}/\Sigma Cr$ values, determined from Ol separates from two lherzolites, one Cpx-rich lherzolite and one wehrlite.

Sample	$H_{1s/4s}$	$Cr^{2+}/\Sigma Cr$	A_{1s-4s}	$Cr^{2+}/\Sigma Cr$
Cl09-65 Ol	0.0555	0.18	0.0743	0.17
Cl09-74 Ol	0.0589	0.20	0.0700	0.16
CLB05-15 Ol	0.0524	0.16	0.0833	0.20
	0.4585	0.14		
Cl09-86 Ol		n.d.		n.d.
Cl09-31 Cpx		n.d.		n.d.
Cl09-31 Opx		n.d.		n.d.
Cl09-65 Cpx		n.d.		n.d.
Cl09-65 Opx		n.d.		n.d.
Cl09-65 Spl		n.d.		n.d.
Cl09-74 Cpx		n.d.		n.d.
Cl09-74 Opx		n.d.		n.d.
Cl09-81 Spl		n.d.		n.d.
CLB05-15 Cpx		n.d.		n.d.

n.d. represents not detected.

Notably, all of four grains with different sizes, randomly-selected from Cl09-62 Opx, display observable elemental zoning of Cr and Al (Fig. 2a, b). By contrast, no systemic zoning profiles of Cr and Al are observed for Cl09-73 Opx (Fig. 2a, b).

5. Discussion

Our isotope measurements indicate that there are resolvable differences in Cr isotope compositions for coexisting mantle minerals. Such inter-mineral isotope fractionation may represent equilibrium or disequilibrium isotope fractionation. To further test these results, we propose a simplified theoretical prediction for inter-mineral Cr isotope fractionation using the ionic model by Macris et al. (2015) and Young et al. (2015), and we examine the factors affecting the inter-mineral Cr isotope fractionation in natural samples.

5.1. Ionic model predictions for equilibrium inter-mineral Cr isotope fractionation

To determine inter-mineral metal isotope fractionation, both direct experimental petrological determination and theoretical calculation were two common methods in addition to natural sample analyses. Taken Fe isotopes as an example, inter-mineral isotope fractionations were experimentally determined (Shahar et al., 2008; Hin et al., 2012; Sossi and O'Neill, 2017). Several theoreti-

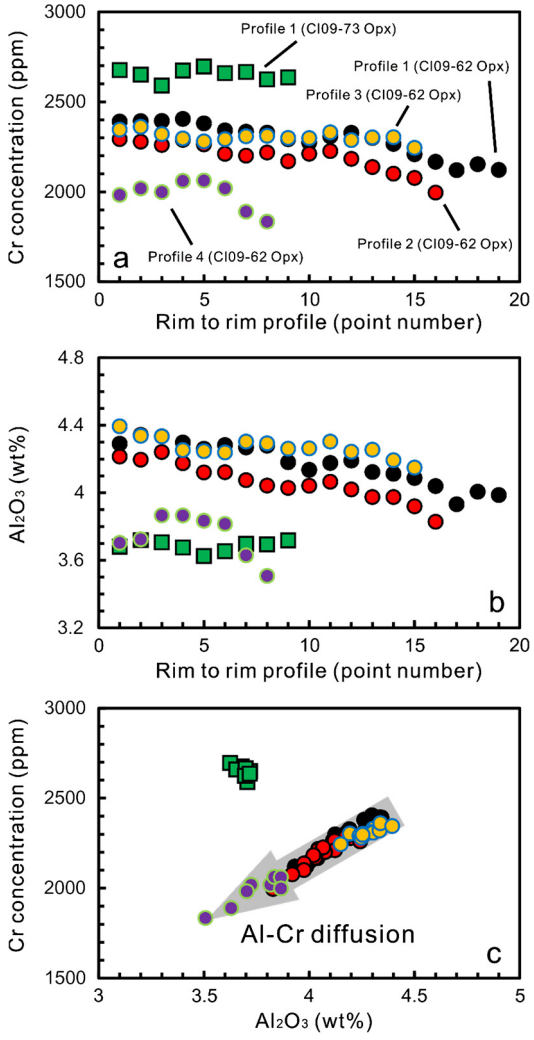

Fig. 2. Concentration zoning of individual Opx grains from Cl09-62 and Cl09-73 for Cr (a) and Al_2O_3 (b) and Al_2O_3–Cr correlations for the five Opx profiles (c). Each distance interval for adjacent two points was approximately ~100 μm.

cal models were proposed to interpret the observed isotope data, such as, the ab-initio method (Blanchard et al., 2009), the Mössbauer/NRIXS methods (Dauphas et al., 2012; Polyakov et al., 2007; Sossi and O'Neill, 2017) and the ionic model (Macris et al., 2015; Young et al., 2009, 2015). Considering that inter-mineral Fe isotope fractionation predicted by the ionic model seems to be most in line with observations of natural mantle minerals (Macris et al., 2015), the ionic model approach combined with the XANES results is attempted to constrain the inter-mineral Cr isotope fractionations.

Based on the isotope theory (Urey, 1947) and the ionic model (Macris et al., 2015; Young et al., 2009, 2015), in the case of high temperature conditions (>600 °C), where quantum effects are small, inter-mineral Cr isotope fractionation can be simply expressed as:

$$\delta^{53}Cr_a - \delta^{53}Cr_b \approx 10^3 \ln \alpha_{a-b}^{53/52} = \frac{10^3}{24}\left(\frac{h}{k_b T}\right)^2 \left(\frac{1}{m_{52}} - \frac{1}{m_{53}}\right)\left[\frac{K_{f,a}}{4\pi^2} - \frac{K_{f,b}}{4\pi^2}\right], \quad (1)$$

where m_{52} and m_{53} are the atomic masses of ^{52}Cr and ^{53}Cr, respectively. In addition, k_b is Boltzmann's constant, h is Planck's constant, and $K_{f,a}$ and $K_{f,b}$ are the average force constants for phases a and b, respectively. We employ an approach similar to that used for Fe isotopes by Macris et al. (2015) to incorporate the influences induced by changes in valence. The average force constants $K_{f,ij}$ can be written as:

$$K_{f,ij} = \frac{z_i z_j e^2 (1-n)}{4\pi \varepsilon_0 r_{ij}^3}, \quad (2)$$

where z_i and z_j are the valences of cation and anion, e is the charge of an electron, ε_0 is the electric constant (vacuum permittivity), r_{ij} is the inter-ionic spacing defined as equilibrium interionic distance between cation i and anion j, and n is the Born–Mayer constant for the repulsion term (empirically equal to 12) (Young et al., 2015). The equilibrium interionic distance r_{ij} is calculated based on effective cationic and anionic radii from Shannon (1976) for a given coordination environment and a cationic valence. Recent work has revealed that effective radii are positively correlated with valences and negatively correlated with coordination numbers (Gibbs et al., 2014), which are used to calculate the effective radii of Cr species in this study. In general, according to the formulas above, we can predict that heavy isotopes concentrate in substances in which the coordination number is low and the valence is high. Before modeling, these two major factors, Cr valence ratios and coordination environments, need to be evaluated in major Cr-bearing mantle minerals.

The proportion of different valence states of Cr (expressed here as the $Cr^{2+}/\Sigma Cr$ ratio) in the mantle minerals mainly depends on the redox condition and equilibrium temperature. Burns and Burns (1975) proposed that all Cr species were expected to occur in the +3 valence state within the range of oxygen fugacity [fayalite–magnetite–quartz (FMQ) −2 to +2 log units] for terrestrial basalts. However, Berry et al. (2006) observed that $Cr^{2+}/\Sigma Cr$ ratios of a quenched basaltic glass vary from ~0.45 at the nickel-nickel oxide (NNO) buffer to ~0.90 at IW buffer at 1400 °C. On the other hand, $Cr^{2+}/\Sigma Cr$ ratios in the mantle were also temperature-dependent, that Cr^{2+} should only be important in mantle peridotite above 1200 °C and predominant above 1500 °C based on thermodynamic data from Li et al. (1995). When temperature decreases, Cr^{2+} becomes unstable due to electron exchange with Fe^{3+} (Berry et al., 2006; Li et al., 1995). Olivine, with the lack of Fe^{3+}, could effectively record the $Cr^{2+}/\Sigma Cr$ ratio of its parental magmatic melt (Bell et al., 2014). For example, $Cr^{2+}/\Sigma Cr$ ratios of Ol from some ureilites could reach ~0.92 at IW-3.1 to IW-2.6 at 1300 °C (Goodrich et al., 2013). Given the more-oxidizing environment of the Earth's upper mantle compared with those of the mantles of ureilite parent bodies (Goodrich et al., 2013), $Cr^{2+}/\Sigma Cr$ ratios of Earth mantle minerals should be lower. This is evidenced by the low $Cr^{2+}/\Sigma Cr$ ratios (0.16 to 0.20) for the measured Ol from both lherzolites and Cpx-rich lherzolites. Furthermore, no Cr^{2+} was detected in Cl09-86 Ol, probably implying that metasomatisms by recycling carbonates lead to oxidation of Cr^{2+} in these wehrlites. Seven Py separates from both lherzolites and Cpx-rich lherzolites have no detectable Cr^{2+}, which is similar to the observation of co-existing Cr^{3+}-dominated Py and Cr^{2+}-dominated Ol in lunar basalts 15555 and 70035 by XANES (Sutton et al., 1993) and Cr^{3+}-dominated Py from the Martian basalt QUE 94201 (Karner et al., 2007). However, an experimental work proposed that Cr^{2+} preferentially enters into Py lattices relative to co-existing Ol under high temperature and reducing conditions in Fe-free systems (Li et al., 1995). Lack of Cr^{2+} in our Py can be the result of electron exchange reaction $Fe^{3+} + Cr^{2+} \rightarrow Fe^{2+} + Cr^{3+}$ due to the presence of Fe^{3+} in natural melts or minerals during cooling from mantle temperatures (~1300 °C) to their equilibration temperatures (~950 °C) (Berry et al., 2006; Li et al., 1995). Thus, taking account of low equilibrium temperatures of the investigated samples, we propose that the obtained $Cr^{2+}/\Sigma Cr$ ratios of the minerals by XANES should represent the lower limits in their original minerals before cooling. However, to

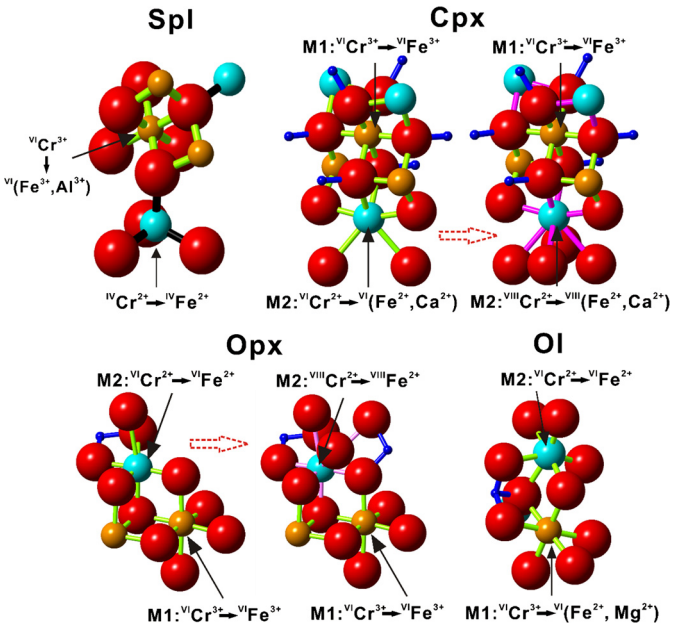

Fig. 3. Crystal structures for Cr-bearing Spl, Cpx, Opx, and Ol displaying nearest neighbors for Cr^{2+} and Cr^{3+} ions. The structures were built using CrystalMaker software based on the effective ionic radii for Cr species with different coordination environments (0.8 Å for 6-coordinated Cr^{2+} and 0.615 Å for 6-coordinated Cr^{3+}) reported by Shannon (1976). Oxygen is shown as large red spheres in all structures, and the small, dark blue spheres represent silicon ions. The orange spheres and the light blue spheres represent the sites for trivalent ions and bivalent ions, respectively. The 4-coordinated, 6-coordinated, and 8-coordinated Cr–O bonds are shown in black, yellow, and purple, respectively. It is noteworthy that Cr^{2+} can substitute in distorted octahedral M2 positions with 6- to 8-coordination in the Cpx and Opx structures. (For interpretation of the colors in the figure(s), the reader is referred to the web version of this article.)

quantitatively determine the initial $Cr^{2+}/\Sigma Cr$ ratios for these Py is very challenging. Although, a prediction of Cr^{2+} preferentially incorporated into Py relative to Ol has been made by Li et al. (1995), their experiments were based on nearly all Cr as Cr^{2+} in crystallized Ol and Py at the Cr–CrO buffer. Under relative oxidizing mantle conditions, the predominant Cr species is Cr^{3+}, which also strongly tends to enter into Py relative to Ol (Duke, 1976), and thus it is difficult to assess the Cr^{2+}/Cr^{3+} differences between Py and Ol. Therefore, in our ionic model, the $Cr^{2+}/\Sigma Cr$ values of natural Opx and Cpx are assumed to vary within a range similar to those of coexisting Ol. The Cr^{2+} component in Spl is generally considered to be limited, and potential Cr^{2+}-bearing species such as Cr_3O_4 is metastable (or stable within a very narrow pressure–temperature range) under mantle conditions. For Spl from mantle xenoliths, as well as from lunar basalts, Cr species is always in +3 valence state calculated from stoichiometry (O'Neill and Navrotsky, 1984), supported by our XANES analyses of Spl separates from two lherzolites (Fig. 1e and f). In the model, we calculate the inter-mineral Cr isotope fractionation assuming $Cr^{2+}/\Sigma Cr$ ratios in Ol and Py ranging from 0 to 1 and 0 for Spl, to assess the effects of Cr valence states on inter-mineral isotope fractionation over a large oxygen fugacity range covering most terrestrial and extraterrestrial conditions.

A comparative study of incorporation of Cr with different valence states into the crystallographic sites of Ol, Py and Spl from planetary basalts has been reported by Papike et al. (2005). Considering that ionic radii of Cr^{2+} and Cr^{3+} (0.80 Å and 0.615 Å) are similar to those of Fe^{2+} and Fe^{3+} (0.78 Å and 0.645 Å) in 6-coordinated sites (Shannon, 1976), individual Cr species were expected to substitute the lattice sites for Fe with same valences. The occupation of Cr in different mineral structures is briefly summarized here (Fig. 3). For Ol with a general formula of $(X_{M2}, Y_{M1})SiO_4$, Cr^{2+}, with a relatively larger ionic radius, is generally incorporated into the M2 octahedron site (6-coordination), whereas smaller Cr^{3+} substitutes the M1-site cation with 6-coordination (Fig. 3, Hanson and Jones, 1998; Papike et al., 2005; Goodrich et al., 2013). The general formula for Py can be written as $X_{M2}Y_{M1}Z_2O_6$. Here, in both mantle Cpx and Opx, Cr^{3+} is proposed to be in the octahedral M1 site (6-coordination) and Cr^{2+} preferentially occupy the distorted M2 site (6–8-coordination) (Burns, 1975), similar to Fe^{2+} occupations in 6–8 coordinated M2 site (Macris et al., 2015). However, it is difficult to assess the individual portions of Cr^{2+} with 6- to 8-coordinations, thus, the M2 site for Cr^{2+} is proposed to have an effective 7-coordination (Fig. 3, Macris et al., 2015). Although Cpx may have a slightly higher $Cr^{2+}/\Sigma Cr$ value than co-existing Opx (Li et al., 1995), there are no observations of notable differences in Cr ionic valences and associated crystallographic sites between them. The typical Spl structure (XY_2O_4) has tetrahedral (4-coordinated) and octahedral (6-coordinated) sites for divalent cation X and trivalent cation Y, respectively. In general, Cr^{3+} occupies the octahedral site, and Cr^{2+} (if present) predominantly occupies the tetrahedral site (Papike et al., 2005). In our model, because we assume that no Cr^{2+} is present in Spl, all Cr^{3+} occupies the octahedral site (Fig. 3).

In brief, the combined charges and coordination numbers of Cr in mantle minerals are summarized as follows: Cr^{2+} and Cr^{3+} in Ol are 6-coordinated; Cr^{3+} is 6-coordinated, and Cr^{2+} is ~7-coordinated in Py; Cr^{3+} in Spl is 6-coordinated. Detailed parameters and fractionation factor calculations are in Table 3 and Appendix B. The estimated inter-mineral Cr isotope fractionation factors are given in Fig. 4a–c. In cases where co-existing Py and Ol have similar and low $Cr^{2+}/\Sigma Cr$ values (e.g., 0 to 0.2, in Fig. 4c), the equilibrium fractionation factors between them are close to 0 from 600 °C to 1200 °C. With respect to the mineral pairs Spl–Ol

Table 3
The $Cr^{2+}/\Sigma Cr$ values in minerals and associated force constants ($K_{f,Cr-O}$) used in the ionic model. The calculated inter-mineral isotope fractionation factors ($\Delta^{53}Cr$) are also presented. The values following in parentheses are the $Cr^{2+}/\Sigma Cr$ values in minerals for calculations.

	$Cr^{2+}/\Sigma Cr$	$K_{f,Cr-O}$ (N/m)	T (°C)		600	700	800	900	1000	1100	1200
Ol	1	979.87	$\Delta^{53}Cr_{Spl-Ol}$	Spl(0)–Ol(1)	0.66	0.53	0.43	0.36	0.31	0.27	0.23
	0.25	1641.16	$\Delta^{53}Cr_{Spl-Ol}$	Spl(0)–Ol(0.25)	0.19	0.16	0.13	0.11	0.09	0.08	0.07
	0.2	1693.93	$\Delta^{53}Cr_{Spl-Ol}$	Spl(0)–Ol(0.15)	0.12	0.10	0.08	0.07	0.06	0.05	0.04
	0.15	1747.94	$\Delta^{53}Cr_{Spl-Ol}$	Spl(0)–Ol(0)	0.00	0.00	0.00	0.00	0.00	0.00	0.00
	0	1917.79	$\Delta^{53}Cr_{Spl-Py}$	Spl(0)–Py(1)	0.76	0.61	0.50	0.42	0.36	0.31	0.27
Py	1	829.2	$\Delta^{53}Cr_{Spl-Py}$	Spl(0)–Py(0.2)	0.19	0.15	0.13	0.11	0.09	0.08	0.07
	0.2	1645.79	$\Delta^{53}Cr_{Spl-Py}$	Spl(0)–Py(0.1)	0.09	0.07	0.06	0.05	0.04	0.04	0.03
	0.1	1785.94	$\Delta^{53}Cr_{Spl-Py}$	Spl(0)–Py(0)	−0.01	−0.01	−0.01	−0.01	−0.01	−0.01	−0.01
	0	1937.14	$\Delta^{53}Cr_{Py-Ol}$	Py(0)–Ol(0)	0.01	0.01	0.01	0.01	0.01	0.01	0.01
Spl	0	1917.79	$\Delta^{53}Cr_{Py-Ol}$	Py(0)–Ol(0.2)	0.17	0.14	0.11	0.09	0.08	0.07	0.06
			$\Delta^{53}Cr_{Py-Ol}$	Py(0.2)–Ol(0.2)	−0.03	−0.03	−0.02	−0.02	−0.02	−0.01	−0.01
			$\Delta^{53}Cr_{Py-Ol}$	Py(0.1)–Ol(0.25)	0.10	0.08	0.07	0.06	0.05	0.04	0.04

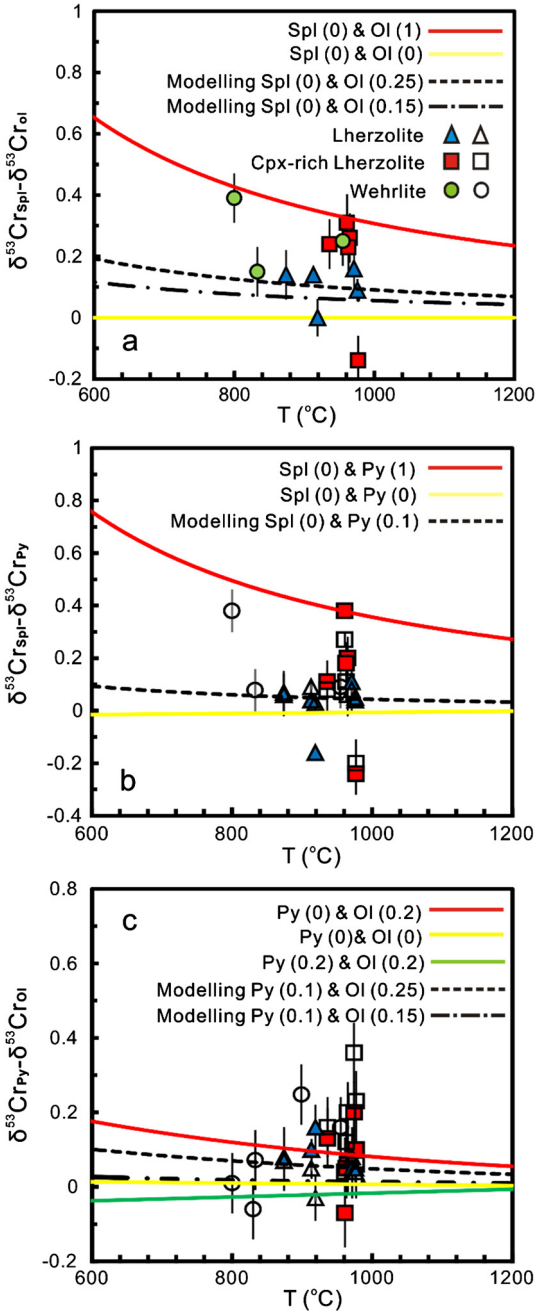

Fig. 4. Calculated inter-mineral equilibrium Cr isotope fractionation factors at different temperatures: (a) $\delta^{53}Cr_{Spl}$–$\delta^{53}Cr_{Ol}$, (b) $\delta^{53}Cr_{Spl}$–$\delta^{53}Cr_{Py}$, and (c) $\delta^{53}Cr_{Py}$–$\delta^{53}Cr_{Ol}$ based on the ionic model. The lines in different colors represent the estimations for the inter-mineral fractionation factors based on different $Cr^{2+}/\Sigma Cr$ values of each mineral, which are expressed as the values following the mineral names in all plots. The filled and open symbols represent Opx-related and Cpx-related mineral pairs, respectively. The dashed and dotted curves in (a) represent calculated equilibrium fractionation factors using XANES-determined Cr valences of Spl and Ol. The dashed and dotted curves in (b) and (c) are calculated equilibrium fractionation factors fitting the observed values by adjusting the $Cr^{2+}/\Sigma Cr$ ratios of Py. Uncertainties quoted for $\Delta^{53}Cr$ in this and all subsequent figures are the square root of the sum of the square of the uncertainty of the two minerals.

and Spl–Py, because of the similar Cr^{3+} coordination environments (6-fold coordination) in all minerals, significantly lower $Cr^{2+}/\Sigma Cr$ (0) in Spl relative to those in Py and Ol will almost always lead to isotopically heavier Cr in Spl than in Ol and Py (Fig. 4a and b).

It should be noted that although Cr is often a trace element in major mantle minerals (except Spl), the effects of Cr concentration on Cr isotope fractionation between different mineral pairs were not taken into consideration at this stage. Overall, the predicted Cr isotope composition among the major mantle minerals in isotopic equilibrium according to the ionic model is $\delta^{53}Cr_{Spl} > \delta^{53}Cr_{Py} \geq \delta^{53}Cr_{Ol}$, which is similar to that for inter-mineral Fe isotope fractionation (Macris et al., 2015).

5.2. Inter-mineral Cr isotope fractionation

Having established a reasonable ionic model for equilibrium Cr isotope fractionation, here, we compare the data from Beiyan lherzolites and metasomatized Cpx-rich lherzolites and wehrlites to better understand the systematics of inter-mineral isotope fractionation as well as the processes (metasomatism, diffusion) that could potentially affect the Cr isotope compositions of minerals.

5.2.1. Chromium isotopic equilibrium in lherzolites

Relative to the Cpx-rich lherzolites and the wehrlites, the lherzolites here are thought to have experienced few or no secondary processes (e.g., metasomatism, alteration) (Xiao et al., 2010, 2013). Except for Cl09-62, inter-mineral Cr isotope fractionation for different mineral pairs is nearly constant among the other four lherzolites (Cl09-31, Cl09-65, Cl09-73, and Cl09-74) (Table 1, Fig. 5a–d), suggesting equilibrium inter-mineral Cr isotope fractionation. For example, co-existing Opx and Cpx mineral pairs in these lherzolites display indistinguishable inter-mineral Cr isotope fractionation (−0.03‰ to 0.05‰, Table 1 and Fig. 5d). With respect to the Spl–Ol pair, inter-mineral Cr isotope fractionation of the four lherzolites is also constant with a mean value of 0.14 ± 0.04‰ (Fig. 5a). Moreover, combined with constant isotope fractionation factors of $\Delta^{53}Cr_{Py-Ol}$ (0.05‰ to 0.10‰) and $\Delta^{53}Cr_{Spl-Py}$ (0.04‰ to 0.11‰), all minerals in these lherzolites are expected to be in Cr isotope equilibrium (Table 1 and Fig. 5b, c).

The equilibrium inter-mineral Cr isotope fractionation can be inferred from two other lines of evidence: (1) the isotope variations in the same mineral type among different samples, such as 0.44‰ for Spl, 0.44‰ for Ol, 0.46‰ for Opx, and 0.42‰ for Cpx, are obviously larger than the variations observed in the inter-mineral isotope fractionation values, because the inter-mineral equilibrium fractionation is temperature-dependent and irrelevant to different samples; (2) the inter-mineral Cr isotope fractionations observed for natural samples and predicted by the ionic model are consistent with each other. First, the constant Cr isotope fractionation (~0) between co-existing Opx and Cpx is in agreement with model predictions of limited equilibrium fractionation because of similar redox states and coordination environments of the Cr ions present. Thus, in the following discussions, both Cpx and Opx are treated as Py. Second, according to the ionic model combined with XANES-determined $Cr^{2+}/\Sigma Cr$ values of Ol separates and equilibrium temperatures for the lherzolites Cl09-74 and Cl09-65, the calculated equilibrium $\Delta^{53}Cr_{Spl-Ol}$ are 0.06‰ to 0.09‰ and 0.06‰ to 0.11‰, respectively. The calculated results are consistent with those measured by both TIMS (0.09 ± 0.04‰ for Cl09-74 and 0.14 ± 0.03‰ for Cl09-65) and MC–ICP–MS (0.09 ± 0.08‰ for Cl09-74) within errors. Although $Cr^{2+}/\Sigma Cr$ ratios of Ol from other two lherzolites (Cl09-31 and Cl09-73) are not directly determined, similar whole-rock oxygen fugacities for these four lherzolites ($\log f_{O_2}$ of −1.39 to −0.66 relative to FMQ buffer, Supplementary Table S1) imply that Ol from Cl09-31 and Cl09-73 likely have similar $Cr^{2+}/\Sigma Cr$ ratios (~0.2). The Spl–Ol fractionation factors predicted by the model and measured (MC–ICP–MS) for Cl09-31 and Cl09-73 are also consistent with each other (Fig. 4a). Finally, based on the $\Delta^{53}Cr_{Spl-Py}$ values, the initial $Cr^{2+}/\Sigma Cr$ ratios of Py in equilibrium with Spl and Ol from these lherzolites are 0.10–0.20 (Fig. 4b, c). These values are in agreement with the prediction in section 5.1, and higher than the XANES data, implying that Cr^{2+} originally in Py was mostly oxidized to Cr^{3+}.

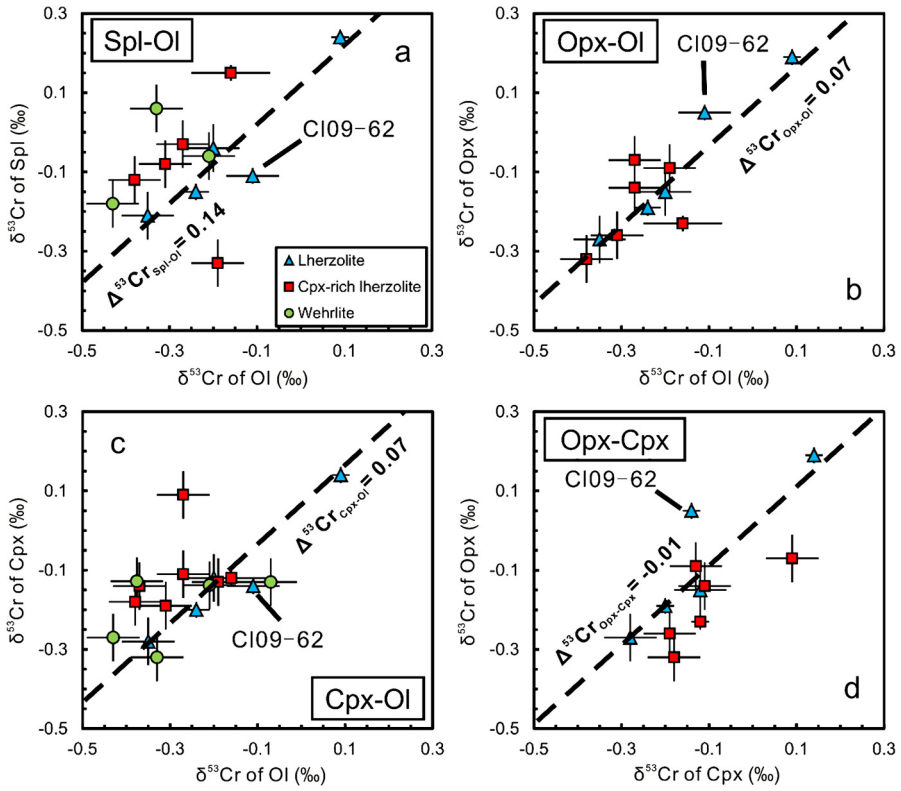

Fig. 5. 'δ–δ' plots showing the isotope fractionation between minerals in Beiyan mantle xenoliths. Error bars for δ^{53}Cr of minerals in this and all subsequent figures are 2SD uncertainties defined in the main text. Solid lines represent the equilibrium fractionation lines defined by the mineral pairs of four lherzolites (see the text for a detailed discussion).

With respect to the lherzolite Cl09-62, all plotted mineral-pair data are distant from the equilibrium inter-mineral isotope fractionation lines defined by the other four lherzolites (Fig. 5a–d). Considering their similar equilibrium temperatures and redox environments (Xiao et al., 2013), these mineral pairs might not have reached isotope equilibrium. Similar major element compositions of minerals between Cl09-62 and other lherzolites rule out metasomatism as the predominant cause. Notably, the order of Opx > Cpx ≥ Spl > Ol in $^{53}Cr/^{52}Cr$ for Cl09-62 was similar to some Mongolia peridotite xenoliths in our recent work, which was interpreted as the result of light ^{52}Cr from Opx preferentially diffusing into melt during mantle upwelling based on Al and Cr elemental zoning in Opx (Press et al., 1986; Xia et al., 2017). Here, we propose that the similar reason has caused disequilibrium inter-mineral Cr isotope fractionation in Cl09-62, as we observed similar Al–Cr diffusion profiles for four randomly-selected Opx grains out of 20 from Cl09-62, but not for Cl09-73 Opx which is expected to be in Cr isotope equilibrium (Fig. 2a–c).

5.2.2. Isotopically disequilibrated Cpx-rich lherzolites and wehrlites

Overall, the Δ^{53}Cr values for different mineral pairs from seven Cpx-rich lherzolites display large variations (Table 1). It should be noted that, three of the seven samples (Cl09-47, Cl09-75 and CLB05-15) have relatively constant inter-mineral Δ^{53}Cr values, e.g., $\Delta^{53}Cr_{Spl-Ol}$ of 0.23‰ to 0.26‰, $\Delta^{53}Cr_{Spl-Opx}$ of 0.11‰ to 0.20‰ and $\Delta^{53}Cr_{Spl-Cpx}$ of 0.06‰ to 0.10‰ (Table 1 and Fig. 5a–d), respectively. However, these fractionations are larger than those for the lherzolites (e.g., Spl–Ol and Spl–Py). Whether these constant values represent inter-mineral equilibrium fractionations can be assessed by combining the results of the ionic models.

The equilibrium temperatures for the Cpx-rich lherzolites (930 °C–970 °C) are similar to those of the lherzolites (870 °C–970 °C) (Supplementary Table S1); thus, temperature effects can be eliminated. Larger equilibrium fractionation factors could potentially be attributed to larger Cr valence differences for the mineral pairs than those for the lherzolites. As described above, Spl in all of our samples have Cr species in the +3 valence state. According to the ionic model, the $\Delta^{53}Cr_{Spl-Ol}$ values of 0.23‰ to 0.26‰ at 930 °C to 970 °C require the $Cr^{2+}/\Sigma Cr$ ratios of Ol achieving approximately 0.6 to 0.9, which is significantly higher than the XANES-determined value of 0.16 ± 0.10 for CLB05-15 Ol. Furthermore, this value is similar to those determined for Ol from some ureilites, for which the oxygen fugacity ($\log f_{O_2}$) was estimated to be −14.2 to −11.4 (IW-3.1 to IW) at 1250 °C (Goodrich et al., 2013), significantly lower than those of Spl-facies upper Mantle (IW+0.6 to IW+5.5, Ballhaus, 1993; Foley, 2010) and the Beiyan Cpx-rich lherzolites (IW+3.1 to IW+4.1). Similarly, high $Cr^{2+}/\Sigma Cr$ values are also required for Opx (up to 0.4) and Cpx (up to 0.2) to explain $\Delta^{53}Cr_{Spl-Opx}$ of 0.11‰ to 0.20‰ and $\Delta^{53}Cr_{Spl-Cpx}$ of 0.06‰ to 0.11‰, which are higher than those of Ol from both lherzolites and Cpx-rich lherzolites (0.14 to 0.20), inconsistent with that Py have lower $Cr^{2+}/\Sigma Cr$ values than co-existing Ol obtained in the isotopically equilibrated lherzolites. Thus, we can conclude that the mineral pairs in these Cpx-lherzolites are out of Cr isotope equilibrium.

With respect to relatively oxidized wehrlites, most Cr species in Ol and Py were in the +3 valence state (e.g., $Cr^{2+}/\Sigma Cr \approx 0$ for Cl09-86 Ol). In this case, the modeling calculations show that the inter-mineral fractionations of Spl–Ol and Py–Ol should be very close to 0 at temperatures >800 °C (Fig. 4a, c). However, large and variable inter-mineral Cr isotope fractionations (e.g., $\Delta^{53}Cr_{Spl-Ol}$ = 0.15‰ to 0.39‰ and $\Delta^{53}Cr_{Cpx-Ol}$ = −0.06‰ to 0.25‰), as well as the highly scattered data in Fig. 4a, c and Fig. 5a, c, indicate that these mineral pairs (Spl–Ol, Py–Ol) are out of Cr isotope equilibrium.

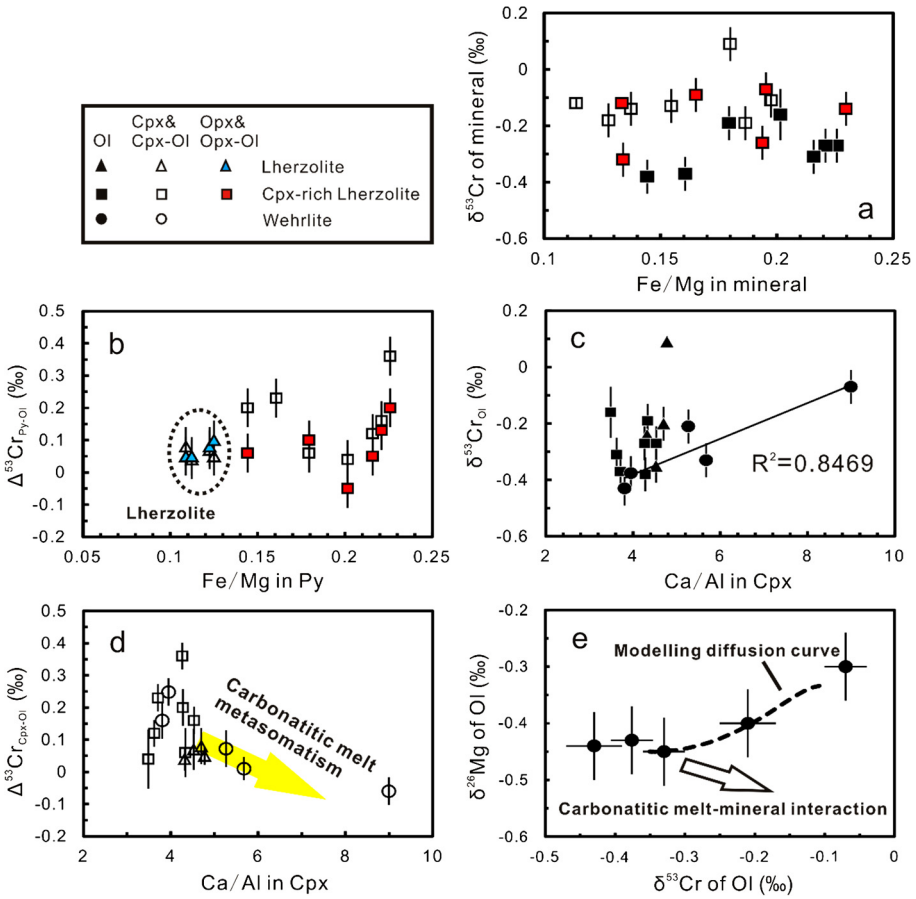

Fig. 6. Plot (a) presents Cr isotope compositions of individual minerals as a function of Fe/Mg mole ratios of these minerals in the Cpx-rich lherzolites. Plot (b) presents the correlations between Cr isotope fractionation values of Py–Ol mineral pairs and Fe/Mg mole ratios of corresponding Py for the lherzolties and Cpx-rich lherzolties. Plot (c) and (d) display the correlations of $\delta^{53}Cr_{Ol}$, $\Delta^{53}Cr_{Cpx-Ol}$ and the Ca/Al ratios of Cpx from the Beiyan peridotites, respectively. Plot (e) presents the positive correlation of the Mg isotope and Cr isotope compositions of Ol from the wehrlites, indicating kinetic diffusion effects rather than the mineral–melt mixing. The $\delta^{26}Mg_{Ol}$ data in (e) are from Xiao et al. (2013). The filled and open symbols in (a)–(e) represent Opx-related and Cpx-related minerals or mineral pairs, respectively. The dotted line in (e) is the calculated diffusion curve according to the model by Richter et al. (1999, 2003). See detailed description in Appendix A.

Relative to the Beiyan lherzolites, the Cpx-rich lherzolites were produced by interaction of lherzolites with evolved silicate melt from asthenosphere, whereas the wehrlites experienced additional metasomatism by recycling sedimentary carbonates associated with the Paleo-Pacific slab subduction, as indicated by carbonate mineral inclusions, positive Ba and Sr anomalies and low Mg isotope compositions (Xiao et al., 2010, 2013). These metasomatisms could be the cause of inter-mineral Cr isotope disequilibrium.

For Cpx-rich lherzolites, the mineral Fe/Mg ratio is used as the index of mafic melt metasomatism as suggested previously (Xiao et al., 2010). Overall, lack of obvious correlations between the $\delta^{53}Cr$ and Fe/Mg for individual minerals (Fig. 6a) suggest that the mafic melt metasomatism have no systematic effects on the Cr isotope compositions of the minerals likely as a result of Cr isotope heterogeneities in the mantle source. Notably, it seems that the metasomatism could lead to disequilibrium inter-mineral isotope fractionations (Cpx–Ol and Opx–Ol), most of which were larger than the equilibrium fractionation factors (Fig. 6b). For the wehrlites, we take the Ca/Al ratio in Cpx as an index of additional carbonatitic melt metasomatism because carbonatitic melts have higher Ca/Al ratios than mantle peridotites and silicate melts (Rudnick et al., 1993). Although Cpx from wehrlites show significantly enhanced Ca/Al ratios (Fig. 6c, d), correlation between Ca/Al ratios and $\delta^{53}Cr$ for Cpx was not observed (not shown here). This could reflect that carbonate incorporations are insufficient to affect Cr isotope compositions of Cpx, because of the significantly lower Cr contents of carbonates (several to tens ppm) than Py (thousands of ppm). However, positive and negative correlations of $\delta^{53}Cr_{Ol}$ (Fig. 6c) and $\Delta^{53}Cr_{Cpx-Ol}$ (Fig. 6d) with Ca/Al ratios of Cpx, are observed, respectively, suggesting that such metasomatism shifts Ol to the isotopically heavier side. This might be attributed to that the sedimentary carbonates in subduction Paleo-Pacific oceanic crust could inherit heavy isotope compositions from the contemporary oxidized seawater (Bonnand et al., 2013; Frei et al., 2009), and Ol has much lower Cr contents than Py and can be more easily altered in terms of Cr isotope composition. The positive shift in $\delta^{53}Cr_{Ol}$ can occur by two means: mixing of Ol with isotopically heavier carbonatitic melt or chemical diffusion of lighter Cr isotopes from Ol into the melt. These two possibilities can be evaluated by adopting the previous Mg isotope results for the same sample set (Xiao et al., 2013). Because of the low $\delta^{26}Mg$ of sedimentary carbonates ($-0.4‰$ to $-5.1‰$, Teng, 2017 and references therein), direct mixing between Ol and carbonatitic melt will cause the former to be enriched in lighter Mg and heavier Cr isotopes (Fig. 6e), inconsistent with the positive correlation of $\delta^{26}Mg_{Ol}$ and $\delta^{53}Cr_{Ol}$ for these wehrlites (Fig. 6e). Therefore, kinetic diffusions of Mg and Cr isotopes could have occurred; that is to say, isotopically light Mg and Cr both diffused from Ol to carbonatitic melt likely because of lower Mg and Cr contents in sedimentary carbonates (Frei et al., 2009; Teng, 2017). This speculation is consistent with the modeling curve of $\delta^{26}Mg$ and $\delta^{53}Cr$ during chemical diffusions from Ol to melt according to Richter et al. (1999, 2003) (Fig. 6e, see detailed calculations in Appendix A).

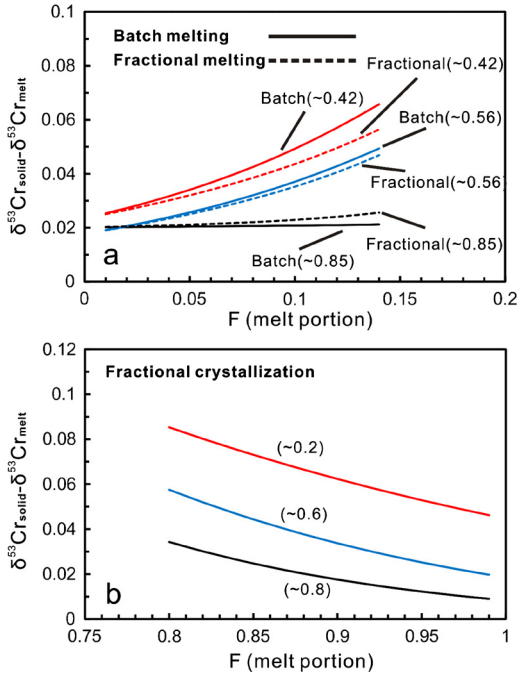

Fig. 7. Plot (a) represents variations of the Cr isotope fractionation between residual solid and melt as a function of melt fraction (F), and initial oxygen fugacities following the non-modal melting model from Sossi and O'Neill (2017) in both batch and fractional melting scenarios. The starting material has a composition of a fertile Spl-facies lherzolite (60% Ol, 24% Opx, 15% Cpx and 1% Spl in volume). The numbers in parentheses are the $Cr^{3+}/\Sigma Cr$ values in the initial peridotites summed over each mineral. In the case of $F = 0.1$, the two melting scenarios with initial $Cr^{3+}/\Sigma Cr$ values of 0.42, 0.56 and 0.85 (all other parameters are kept constant) would generate mafic melts with $Cr^{3+}/\Sigma Cr$ of 0.13–0.15, 0.21–0.24 and 0.55–0.6, corresponding to oxygen fugacities of ~IW, ~IW+1.2 and ~IW + 3.8 at 1400 °C (Berry et al., 2006), respectively, which cover the oxygen fugacity range covering most terrestrial and extraterrestrial conditions [e.g., basaltic melts from Moon (IW-2 to IW), from Mars (IW to IW+2), from Earth (IW+2 to IW+6), Papike et al., 2005]. Plot (b) represents variations of the Cr isotope fractionation between crystallized phase (consisting of Ol and Spl/Chromite in 99:1 volume ratio) and melt as a function of melt fraction (F) and initial oxygen fugacities during partial crystallization of a basaltic magma. The values in parentheses are the $Cr^{3+}/\Sigma Cr$ values (0.2, 0.6 and 0.8) in the initial MORB-like melts with oxygen fugacities of IW+0.9, IW+4 and IW+5.7 (Berry et al., 2006), respectively. Detailed calculation methods and parameters are given in Appendix A.

5.3. Implications on Cr isotope fractionation during high-temperature processes

The observation of the equilibrium inter-mineral Cr isotope fractionation order ($\delta^{53}Cr_{Spl} > \delta^{53}Cr_{Py} \geq \delta^{53}Cr_{Ol}$), based on both laboratory observations and ion modeling predictions, provides important constraints on Cr isotope behavior during high-temperature petrologic processes, particularly during partial melting and fractional crystallization.

During partial melting of a Spl-facies peridotite at the Spl stable pressure of ~1 to 2.5 GPa, a general order of mineral consumption is Py, Spl and finally Ol (Walter and Presnall, 1994; Walter, 2003). Here, we present a non-modal melting approach following Sossi and O'Neill (2017). Detailed methods and parameters were given in Appendix A. Briefly, according to a melting reaction of 0.15 Opx + 1 Cpx = 0.15 Ol + 1 melt (Walter, 2003), the melts are always Cr isotopically lighter than the residual phases in both fractional and batch melting scenarios (Fig. 7a). The Cr isotope fractionations are similar at low partial melting degrees for the two scenarios, while enhanced differences could be resulted from higher melting degrees. As shown in Fig. 7a, redox states of the sources have notable effects on the Cr isotope fractionation. Larger isotope fractionations occur under more reducing conditions. These phenomena are associated with larger force constant differences between Cr^{3+}-dominated Spl in the solids and lower $Cr^{2+}/\Sigma Cr$ values of the melts from more reducing sources. Generally, the calculated isotope fractionation trend is consistent with observations of some slightly isotopically heavier refractory peridotites reported by Xia et al. (2017). Considering the high oxygen fugacity conditions of the Earth's upper mantle, the solid-melt fractionation factor is small, thereby leading to limited Cr isotope variations in mantle rocks (Schoenberg et al., 2008; Xia et al., 2017).

Bonnand et al. (2016) obtained positive correlations of whole-rock Cr contents and isotope compositions with Mg# values of mare basalts, which were interpreted as a result of fractional crystallization of isotopically heavier Spl from basaltic magma with an equilibrium fractionation factor ($\Delta^{53}Cr_{solid\text{-}melt}$) of 0.05–0.15‰. According to our modeling results (Fig. 7b), the fractionation would require $Cr^{2+}/\Sigma Cr$ ratios in lunar basaltic magma higher than 0.8 at a temperature of 1300 °C, which is in line with an empirical estimation of ~0.9 based on experimentally determined correlations of $Cr^{2+}/\Sigma Cr$ values and oxygen fugacities in mafic melts (Berry et al., 2006), given the low oxygen fugacity of the moon mantle (IW-2 to IW) (Wadhwa, 2008 and references therein).

In this study, we have demonstrated that Cr isotopes can be fractionated at the mineral scale under high-temperature conditions likely because of differences in the redox state and the coordination environment of Cr between different minerals. This finding warrants further studies on Cr isotope behavior during planetary lithology evolutions, particularly where changes in redox conditions are involved.

6. Conclusion

This paper reports the first systematic attempt at exploring Cr isotope fractionation between coexisting mantle minerals by combining ionic model predictions and natural sample analyses. The major conclusions are as follows:

1. We developed an ionic model to make predictions about the general magnitude of inter-mineral equilibrium Cr isotope fractionations. The inter-mineral Cr isotope fractionation depends on both the coordination environment and the $Cr^{2+}/\Sigma Cr$ value of the minerals, and different oxidation states are often accompanied by changes in coordination number for Cr^{2+} and Cr^{3+}. A general order of $\delta^{53}Cr_{Spl} > \delta^{53}Cr_{Py} \geq \delta^{53}Cr_{Ol}$ is achieved, which could provide reasonable interpretations for observations of Cr isotope fractionation during partial melting and fractional crystallization.
2. Constant inter-mineral Cr isotope fractionation factors for different mineral pairs (Spl–Ol, Py–Ol, Spl–Py, and Opx–Cpx) from Beiyan lherzolites suggest that the minerals are in Cr isotope equilibrium. These values are in excellent agreement with the ionic model predictions combining with XANES-determined $Cr^{2+}/\Sigma Cr$ values for minerals from these lherzolites. The disequilibrium inter-mineral Cr isotope fractionation for Beiyan Cpx-rich lherzolites and wehrlites is likely attributable to metasomatisms by means of mineral–melt interaction and/or kinetic diffusion.

Acknowledgements

We thank the staff at the Beijing Synchrotron Radiation Facility (BSRF) in China. We also thank Zhenhui Hou and Qiongxia Xia for their assistances with ICP-MS and EPMA analyses. Constructive comments given by Editor Frederic Moynier, Paolo Sossi and two anonymous reviewers have improved the quality of the manuscript greatly. This work was supported by the National

Key R&D Program of China (2016YFC0600404) and Strategic Priority Research Program (B) of Chinese Academy of Sciences (Grant No. XDB18000000), the Chinese Ministry of Science and Technology (2015CB856102), the National Natural Science Foundation of China (41403001, 41673006) to Ji Shen, and the National Natural Science Foundation of China (41625013, 41473066, 41571130052) to Liping Qin.

Appendix. Supplementary material

Supplementary material related to this article can be found online at https://doi.org/10.1016/j.epsl.2018.07.041.

References

Ballhaus, C., 1993. Redox states of lithospheric and asthenospheric upper mantle. Contrib. Mineral. Petrol. 114, 331–348.
Bell, A., Burger, P., Le, L., Shearer, C., Papike, J., Sutton, S., Newville, M., Jones, J., 2014. XANES measurements of Cr valence in olivine and their applications to planetary basalts. Am. Mineral. 99, 1404–1412.
Berry, A.J., O'Neill, H.S.C., 2004. A XANES determination of the oxidation state of chromium in silicate glasses. Am. Mineral. 89, 790–798.
Berry, A.J., O'Neill, H.S.C., Scott, D.R., Foran, G.J., Shelley, J., 2006. The effect of composition on Cr^{2+}/Cr^{3+} in silicate melts. Am. Mineral. 91, 1901–1908.
Blanchard, M., Poitrasson, F., Méheut, M., Lazzeri, M., Mauri, F., Balan, E., 2009. Iron isotope fractionation between pyrite (FeS_2), hematite (Fe_2O_3) and siderite ($FeCO_3$): a first-principles density functional theory study. Geochim. Cosmochim. Acta 73, 6565–6578.
Bonnand, P., James, R.H., Parkinson, I.J., Connelly, D.P., Fairchild, I.J., 2013. The chromium isotopic composition of seawater and marine carbonates. Earth Planet. Sci. Lett. 382, 10–20.
Bonnand, P., Parkinson, I.J., Anand, M., 2016. Mass dependent fractionation of stable chromium isotopes in mare basalts: implications for the formation and the differentiation of the Moon. Geochim. Cosmochim. Acta 175, 208–221.
Burns, R.G., 1975. Crystal field effects in chromium and its partitioning in the mantle. Geochim. Cosmochim. Acta 39, 857–864.
Burns, V.M., Burns, R.G., 1975. Mineralogy of chromium. Geochim. Cosmochim. Acta 39, 903–910.
Dauphas, N., Roskosz, M., Alp, E., Golden, D., Sio, C., Tissot, F., Hu, M., Zhao, J., Gao, L., Morris, R., 2012. A general moment NRIXS approach to the determination of equilibrium Fe isotopic fractionation factors: application to goethite and jarosite. Geochim. Cosmochim. Acta 94, 254–275.
Duke, J., 1976. Distribution of the period four transition elements among olivine, calcic clinopyroxene and mafic silicate liquid: experimental results. J. Petrol. 17, 499–521.
Eeckhout, S.G., Bolfan-Casanova, N., McCammon, C., Klemme, S., Amiguet, E., 2007. XANES study of the oxidation state of Cr in lower mantle phases: periclase and magnesium silicate perovskite. Am. Mineral. 92, 966–972.
Farkaš, J., Chrastný, V., Novák, M., Čadkova, E., Pašava, J., Chakrabarti, R., Jacobsen, S.B., Ackerman, L., Bullen, T.D., 2013. Chromium isotope variations ($\delta^{53/52}$Cr) in mantle-derived sources and their weathering products: implications for environmental studies and the evolution of $\delta^{53/52}$Cr in the Earth's mantle over geologic time. Geochim. Cosmochim. Acta 123, 74–92.
Foley, S.F., 2010. A reappraisal of redox melting in the Earth's mantle as a function of tectonic setting and time. J. Petrol. 52, 1363–1391.
Frei, R., Gaucher, C., Poulton, S.W., Canfield, D.E., 2009. Fluctuations in Precambrian atmospheric oxygenation recorded by chromium isotopes. Nature 461, 250–253.
Gibbs, G.V., Ross, N.L., Cox, D.F., Rosso, K.M., Iversen, B.B., Spackman, M., 2014. Pauling bond strength, bond length and electron density distribution. Phys. Chem. Miner. 41, 17–25.
Goodrich, C.A., Sutton, S.R., Wirick, S., Jercinovic, M.J., 2013. Chromium valences in ureilite olivine and implications for ureilite petrogenesis. Geochim. Cosmochim. Acta 122, 280–305.
Hanson, B., Jones, J.H., 1998. The systematics of Cr^{3+} and Cr^{2+} partitioning between olivine and liquid in the presence of spinel. Am. Mineral. 83, 669–684.
Hin, R.C., Schmidt, M.W., Bourdon, B., 2012. Experimental evidence for the absence of iron isotope fractionation between metal and silicate liquids at 1 GPa and 1250–1300 °C and its cosmochemical consequences. Geochim. Cosmochim. Acta 93, 164–181.
Ionov, D., Wood, B., 1992. The oxidation state of subcontinental mantle: oxygen thermobarometry of mantle xenoliths from central Asia. Contrib. Mineral. Petrol. 111, 179–193.
Karner, J., Papike, J., Sutton, S., Shearer, C., McKay, G., Le, L., Burger, P., 2007. Valence state partitioning of Cr between pyroxene–melt: effects of pyroxene and melt composition and direct determination of Cr valence states by XANES. Application to Martian basalt QUE 94201 composition. Am. Mineral. 92, 2002–2005.
Li, J.-P., O'Neil, H.S.C., Seifert, F., 1995. Subsolidus phase relations in the system MgO–SiO_2–Gr–O in equilibrium with metallic Cr, and their significance for the petrochemistry of chromium. J. Petrol. 36, 107–132.
Macris, C.A., Manning, C.E., Young, E.D., 2015. Crystal chemical constraints on intermineral Fe isotope fractionation and implications for Fe isotope disequilibrium in San Carlos mantle xenoliths. Geochim. Cosmochim. Acta 154, 168–185.
McKeown, D.A., Buechele, A.C., Tappero, R., McCoy, T.J., Gardner-Vandy, K.G., 2014. X-ray absorption characterization of Cr in forsterite within the MacAlpine Hills 88136 EL3 chondritic meteorite. Am. Mineral. 99, 190–197.
Moynier, F., Yin, Q.-Z., Schauble, E., 2011. Isotopic evidence of Cr partitioning into Earth's core. Science 331, 1417–1420.
O'Neill, H.S.C., Navrotsky, A., 1984. Cation distributions and thermodynamic properties of binary spinel solid solutions. Am. Mineral. 69, 733–753.
Papike, J., Karner, J., Shearer, C., 2005. Comparative planetary mineralogy: valence state partitioning of Cr, Fe, Ti, and V among crystallographic sites in olivine, pyroxene, and spinel from planetary basalts. Am. Mineral. 90, 277–290.
Polyakov, V., Clayton, R., Horita, J., Mineev, S., 2007. Equilibrium iron isotope fractionation factors of minerals: reevaluation from the data of nuclear inelastic resonant X-ray scattering and Mössbauer spectroscopy. Geochim. Cosmochim. Acta 71, 3833–3846.
Press, S., Wirr, G., Seck, H.A., Eonov, D., Kovalenko, V.I., 1986. Spinel peridotite xenoliths from the Tariat Depression, Mongolia. I: Major element chemistry and mineralogy of a primitive mantle xenolith suite. Geochim. Cosmochim. Acta 50, 2587–2599.
Qin, L., Alexander, C.M.D., Carlson, R.W., Horan, M.F., Yokoyama, T., 2010. Contributors to chromium isotope variation of meteorites. Geochim. Cosmochim. Acta 74, 1122–1145.
Richter, F.M., Davis, A.M., Depaolo, D.J., Watson, E.B., 2003. Isotope fractionation by chemical diffusion between molten basalt and rhyolite. Geochim. Cosmochim. Acta 67, 3905–3923.
Richter, F.M., Liang, Y., Davis, A.M., 1999. Isotope fractionation by diffusion in molten oxides. Geochim. Cosmoch. Acta 63, 2853–2861.
Rudnick, R.L., McDonough, W.F., Chappell, B.W., 1993. Carbonatite metasomatism in the northern Tanzanian mantle: petrographic and geochemical characteristics. Earth Planet. Sci. Lett. 114, 463–475.
Schoenberg, R., Zink, S., Staubwasser, M., Von Blanckenburg, F., 2008. The stable Cr isotope inventory of solid Earth reservoirs determined by double spike MC–ICP–MS. Chem. Geol. 249, 294–306.
Shahar, A., Young, E.D., Manning, C.E., 2008. Equilibrium high-temperature Fe isotope fractionation between fayalite and magnetite: an experimental calibration. Earth Planet. Sci. Lett. 268, 330–338.
Shannon, R.D., 1976. Revised effective ionic radii and systematic studies of interatomic distances in halides and chalcogenides. Acta Crystallogr. 32, 751–767.
Shen, J., Liu, J., Qin, L., Wang, S.J., Li, S., Xia, J., Ke, S., Yang, J., 2015. Chromium isotope signature during continental crust subduction recorded in metamorphic rocks. Geochem. Geophys. Geosyst. 16, 3840–3854.
Sossi, P.A., O'Neill, H.S.C., 2017. The effect of bonding environment on iron isotope fractionation between minerals at high temperature. Geochim. Cosmochim. Acta 196, 121–143.
Sutton, S., Jones, K., Gordon, B., Rivers, M., Bajt, S., Smith, J., 1993. Reduced chromium in olivine grains from lunar basalt 15555: X-ray absorption near edge structure (XANES). Geochim. Cosmochim. Acta 57, 461–468.
Teng, F.-Z., 2017. Magnesium isotope geochemistry. Rev. Mineral. Geochem. 82, 219–287.
Trinquier, A., Birck, J.-L., Allègre, C.J., 2008. High-precision analysis of chromium isotopes in terrestrial and meteorite samples by thermal ionization mass spectrometry. J. Anal. At. Spectrom. 23 (12), 1565–1574.
Urey, H.C., 1947. The thermodynamic properties of isotopic substances. J. Chem. Soc. (Resumed), 562–581.
Wadhwa, M., 2008. Redox conditions on small bodies, the Moon and Mars. Rev. Mineral. Geochem. 68, 493–510.
Walter, M., 2003. Melt extraction and compositional variability in mantle lithosphere. Treatise Geochem. 2, 568.
Walter, M.J., Presnall, D.C., 1994. Melting behavior of simplified lherzolite in the system CaO–MgO–Al_2O_3–SiO_2–Na_2O from 7 to 35 kbar. J. Petrol. 35, 329–359.
Wells, P.R., 1977. Pyroxene thermometry in simple and complex systems. Contrib. Mineral. Petrol. 62, 129–139.
Xia, J., Qin, L., Shen, J., Carlson, R.W., Ionov, D.A., Mock, T.D., 2017. Chromium isotope heterogeneity in the mantle. Earth Planet. Sci. Lett. 464, 103–115.
Xiao, Y., Teng, F.-Z., Zhang, H.-F., Yang, W., 2013. Large magnesium isotope fractionation in peridotite xenoliths from eastern North China craton: product of melt–rock interaction. Geochim. Cosmochim. Acta 115, 241–261.
Xiao, Y., Zhang, H.-F., Fan, W.-M., Ying, J.-F., Zhang, J., Zhao, X.-M., Su, B.-X., 2010. Evolution of lithospheric mantle beneath the Tan–Lu fault zone, eastern North China Craton: evidence from petrology and geochemistry of peridotite xenoliths. Lithos 117, 229–246.
Xu, Z., Zhao, Z.-F., Zheng, Y.-F., 2012. Slab–mantle interaction for thinning of cratonic lithospheric mantle in North China: geochemical evidence from Cenozoic continental basalts in central Shandong. Lithos 146, 202–217.

Young, E.D., Manning, C.E., Schauble, E.A., Shahar, A., Macris, C.A., Lazar, C., Jordan, M., 2015. High-temperature equilibrium isotope fractionation of non-traditional stable isotopes: experiments, theory, and applications. Chem. Geol. 395, 176–195.

Young, E.D., Tonui, E., Manning, C.E., Schauble, E., Macris, C.A., 2009. Spinel-olivine magnesium isotope thermometry in the mantle and implications for the Mg isotopic composition of Earth. Earth Planet. Sci. Lett. 288, 524–533.